IOP Publishing *Plasma Sources Sci. Technol.* **35** (2026) 035007 https://doi.org/10.1088/1361-6595/ae4e06

Plasma Sources Science and Technology

RECEIVED
9 October 2025

REVISED
19 December 2025

ACCEPTED FOR PUBLICATION
5 March 2026

PUBLISHED
16 March 2026

PAPER

Dynamics of argon metastables in Ar–CH_4 radio frequency capacitively-coupled plasma: real-time monitoring with neural network-augmented broadband optical emission spectroscopy

Shurik Yatom[*], **Sophia Gershman** and **Yevgeny Raitses**

Princeton Plasma Physics Laboratory, Princeton University, Princeton, NJ 08543, United States of America
[*] Author to whom any correspondence should be addressed.

E-mail: syatom@pppl.gov

Keywords: argon metastables, RF capacitively coupled plasma, laser-induced fluorescence, machine learning, optical emission spectroscopy, methane plasma chemistry, real time plasma diagnostics

Abstract

In moderate-pressure radio frequency (RF) capacitively coupled plasmas generated in argon–methane mixtures, the density of argon metastable atoms (Ar 1 s_5) exhibits a non-monotonic dependence on methane (CH_4) concentration. Laser-induced fluorescence (LIF) was used to measure and compare local Ar 1 s_5 densities in Ar and Ar–CH_4 plasmas at 2.6 Torr and RF powers of 17–117 W. The addition of 1% CH_4 increases the metastable density, and 2% CH_4 triggers a strong depletion by an order of magnitude, compared to 1% CH_4 case. This non-monotonic behavior demonstrates the sensitivity of metastable populations to small gas admixtures, which is critical for processes where metastables drive precursor dissociation. For real-time monitoring of metastable population, broadband optical emission spectroscopy (OES) is augmented with a feedforward neural network (NN) to predict Ar $s1_5$ densities from spectral features. When trained on LIF data, the NN replicates the absolute densities and the dynamic trends of Ar 1 s_5 density variation. The NN-augmented broadband OES approach can be used as a simple and cost-effective tool for tracking Ar metastables in Ar-rich plasmas, facilitating industrial-scale optimization.

1. Introduction

Moderate-pressure radio frequency (RF) capacitively-coupled plasmas (CCPs) generated in continuous flow-through reactors are widely used for the synthesis of nanoparticles [1–5]. This is because RF CCPs flow reactors are simple, low-cost, and can achieve high production rates of a diverse range of materials (oxides, sulfides, nitrides, and phosphides—as well as elemental Group IV semiconductors) [1, 6–17], and offer straightforward methods for material collection and post-synthesis processing, including integration with 3D printing [6, 7].

Control of material properties in RF CCP flow reactors depends on a detailed understanding and manipulation of plasma chemistry. While process parameters such as input power, gas pressure, and flow rates are readily controlled, the complex interplay between these parameters and the plasma densities of critical reactive species remains an active area of investigation. The reactors often operate with significant amounts of inert gases, which enables easier ignition and assists discharge stability. Among these species, the electronically excited, long-lived states of rare gases, known as metastable atoms, play a pivotal role that is often disproportionate to their relative density [18].

In discharges containing argon, the Ar $1s_5$ and Ar $1s_3$ metastable states, with respective energies of 11.55 eV and 11.72 eV, act as significant reservoirs and carriers of energy. Due to their long lifetimes, these metastables mediate key reaction pathways. Their influence is multifaceted, affecting the overall discharge kinetics through Penning ionization of background or precursor gases and driving the dissociation of molecular precursors essential for film deposition or etching [19].

The importance of argon metastables for plasma chemistry, film deposition [8, 20–22] and carbon nanosynthesis, including in RF CCP plasma [23] is featured widely in literature. A canonical example is the deposition of amorphous hydrogenated silicon (a-Si:H) from silane (SiH_4) and argon mixtures. In this system, the SiH_3 radical is widely recognized as the primary precursor for the growth of high-quality films, owing to its relatively low surface-sticking coefficient, which promotes surface diffusion and network relaxation [24]. The Penning dissociation of SiH_4 by an argon metastable (Ar $1s_5 + SiH_4 \rightarrow Ar + SiH_3 + H$) provides a highly efficient and selective channel for the production of these SiH_3 radicals, a pathway that has been extensively characterized [20]. Consequently, the density of Ar metastables directly influences the population of the dominant film precursors and, by extension, the growth rate and quality of the resulting material [8]. The metastable population is also susceptible to the plasma chemistry; the introduction of molecular gases leads to a rapid depletion, or 'quenching,' of the metastable states, a phenomenon that has been experimentally observed and can serve as a sensitive indicator of plasma process conditions [21, 25].

To quantify the role of these species, *in situ* diagnostics are required. Tunable diode laser absorption spectroscopy (TDLAS) is a non-intrusive technique for measuring the absolute, line-of-sight density of metastables [26]. Laser-induced fluorescence (LIF) is another widely used approach to active spectroscopy in plasmas [27, 28] and gases [29, 30], measuring densities of atoms and molecules [31–36], ions and their temperatures[37],velocities [38–42], and densities of Ar [25, 43] or He [44, 45] metastables. LIF is characterized by its low detection threshold and high spatio-temporal resolution.

Despite the insights provided by TDLAS and LIF, their implementation in RF CCP reactors is often complicated by limited optical access, the need for specialized laser systems, precise optical alignment, and time-intensive data analysis. Optical emission spectroscopy (OES), in contrast, offers a simpler, non-intrusive alternative, capturing broadband emission from excited Ar states that indirectly reflect metastable dynamics through the excitation and de-excitation processes [46]. However, the interpretation of OES data to quantify metastable densities analytically is not straightforward because it is complicated by the nonlinear interplay of the electron energy distributions, quenching rates, and gas admixtures. Traditional approaches rely on complex Collisional-radiative models (CRMs), which are computationally intensive and require a comprehensive set of electron-impact cross-sections that are often unavailable or uncertain.

Machine learning (ML) emerges as a promising tool to overcome these challenges by using complex mappings from OES spectral features to metastable densities, bypassing the need for detailed kinetic models. In low-temperature plasma systems, ML has been applied to predict plasma parameters [47], electron energy distribution functions (EEDFs) [48], and species compositions [49] and molecular temperatures [50], demonstrating its ability to handle high-dimensional, noisy data. By training on calibrated measurements, ML models can enable rapid inference of Ar $1s_5$ densities from routine OES, facilitating process optimization in RF CCP reactors with Ar-based chemistries, such as those involving CH_4 for carbon or SiC synthesis.

In this work, we use a neural network (NN) approach to predict Ar $1s_5$ concentrations for different plasma conditions in an RF CCP reactor based on Ar emission lines extracted from the routine OES. The NN is trained on robust LIF measurements for the same RF CCP device. Hence, this data-driven approach leverages the simplicity of OES by training an NN on high-fidelity LIF data, effectively creating a 'virtual sensor' that can predict Ar $1s_5$ densities in real-time from simple spectral measurements. Such a tool is crucial for optimizing and controlling plasma processes like nanomaterial synthesis, where metastable dynamics directly influence material properties [51, 52].

This paper is organized as follows. Section 2 describes the experimental setup, including the plasma reactor and the LIF and OES diagnostics. Section 3 presents the experimental results, beginning with the measured dynamics of the Ar $1s_5$ population, analysis of the electron temperature, followed by details of the development and performance of the NN model. Section 4 discusses the results and mechanisms behind the observed metastable behavior. Section 5 provides concluding remarks on the significance of these findings and the utility of the NN-augmented OES approach. Three appendices are included for additional detail: appendix A justifies the dominance of stepwise excitation from the Ar $1s_5$ metastable state to the radiating 2p levels under the conditions studied (the physical foundation of the NN approach); appendix B provides an extended discussion of the Corona-model assumptions, line-ratio electron-temperature estimates, and their limitations; appendix C contains the tables with complete neural-network hyper-parameter search.

Table 1. Applied vs measured power for investigated plasma conditions.

Applied power (W)	Measured power (W) Ar	Measured power (W) Ar + 1%CH_4	Measured power (W) Ar + 2%CH_4	Measured power (W) Ar + 5%CH_4
50	33	22	20	17
65	46	35	26	20
80	56	40	39	37
100	64	48	47	40
120	75	60	57	45
150	87	74	70	61
175	94	81	80	70
200	117	102	87	76

2. Experimental

This study employs a combination of LIF and broadband OES to measure the density of Ar 1s_5 metastable atoms in a RF capacitively coupled plasma (CCP) reactor operating with Ar–CH_4 gas mixtures at 2.6 Torr. The experimental setup is detailed in the following subsections.

2.1. Plasma reactor

A 13.65 MHz RF CCP was generated in a flow-through tubular reactor, consisting of a quartz tube, measuring 23.5 cm in length, 1.27 cm in outer diameter, and two copper electrodes, 1 cm wide, wrapped over the quartz tube, 3.5 cm apart. Gas flow was controlled by mass flow controllers (Alicat Inc.), providing 47.5–50 sccm of argon and 0–2.5 sccm of methane, with total flow always equal to 50 sccm. The total pressure in the reactor was maintained at 2.6 Torr. Power was supplied via an RF power source (AG0313, T&C Power Conversion). An impedance matching network and a bi-directional coupler were employed to minimize the reflected power. A Tektronix P6015A, 75 MHz high voltage probe, was used to measure the voltage at the powered electrode, and a Pearson 2877 current monitor measured current to ground. Details on electrical measurements can be found in [51]. To find the average power, the instantaneous power, $P = \mathrm{VI}$, where V is the voltage at the powered electrode and I is the current to ground, was integrated and averaged over time. The result is the average power dissipated by the discharge, provided the current to ground accurately represents the discharge current [53]. This calculation underestimates the discharge power if the plasma plume extends beyond the electrodes. The applied vs measured power is given in table 1. In this work, all results are presented as a function of the average measured power.

2.2. LIF setup

The laser diagnostic system uses an Nd: YAG laser (Continuum Powerlite 8020) that emits nanosecond pulses at 1064 nm with a 20 Hz repetition rate. Equipped with second- and third-harmonic generators, it produces 355 nm pulses to pump an optical parametric oscillator (OPO, Continuum, Horizon), which generates tunable laser pulses. For this experiment, the OPO was set to 696.7 nm, delivering pulses with a 3.92 ns FWHM duration and 4.8 mJ energy. The laser bandwidth at this wavelength is 200 pm. In this work, we employed a planar LIF (pLIF) approach to acquire 2D fluorescence images. The beam was attenuated to 0.7 mJ with an optical density filter (Thorlabs), expanded by a 2 lens Keplerian telescope, then directed into the reactor tube from above using mirrors, and focused on the target volume with a 5 cm focal length cylindrical lens, forming a laser sheath in the plane of interest, having a length of 10.5 mm and width of ~398 μm in the focal plane. The beam passed through the tube, from top to bottom, was refocused with a lens, and then terminated by a beam dump. The setup is illustrated in figure 1. Fluorescence was detected perpendicular to the beam using an iCCD camera (PiMAX4, Princeton Instruments) with a 730 nm spectral filter (10 nm FWHM) and an objective lens. The camera operated with a 100 ns gate, accumulating 100–500 signals per measurement, depending on the experimental condition. A pulse delay generator (Berkley Nucleonics 575) synchronized the camera gate with the laser pulse. For LIF calibration via Rayleigh scattering, the spectral filter was removed to detect the elastic scattering of the 696.7 nm photons.

The LIF approach to measure the density of the Ar1s_5 metastable level was described in detail in our previous work [25], where we described the technical details of the involved measurements, population dynamics modeling, and computations. The diagnostic approach involved a multi-step process combining laser spectroscopy, absolute calibration via Rayleigh scattering, and a kinetic model of the atomic

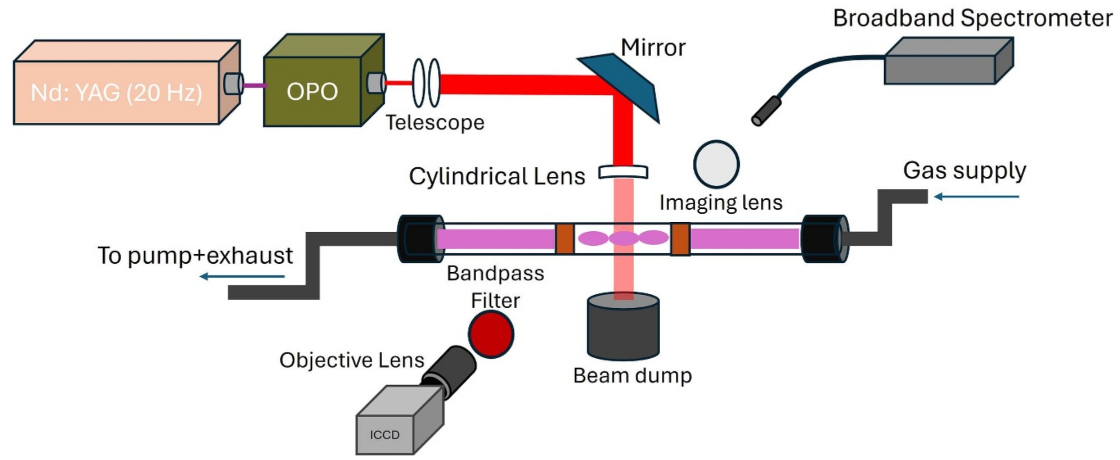

Figure 1. Experimental setup for LIF and broadband spectroscopy of the RF flow-through reactor.

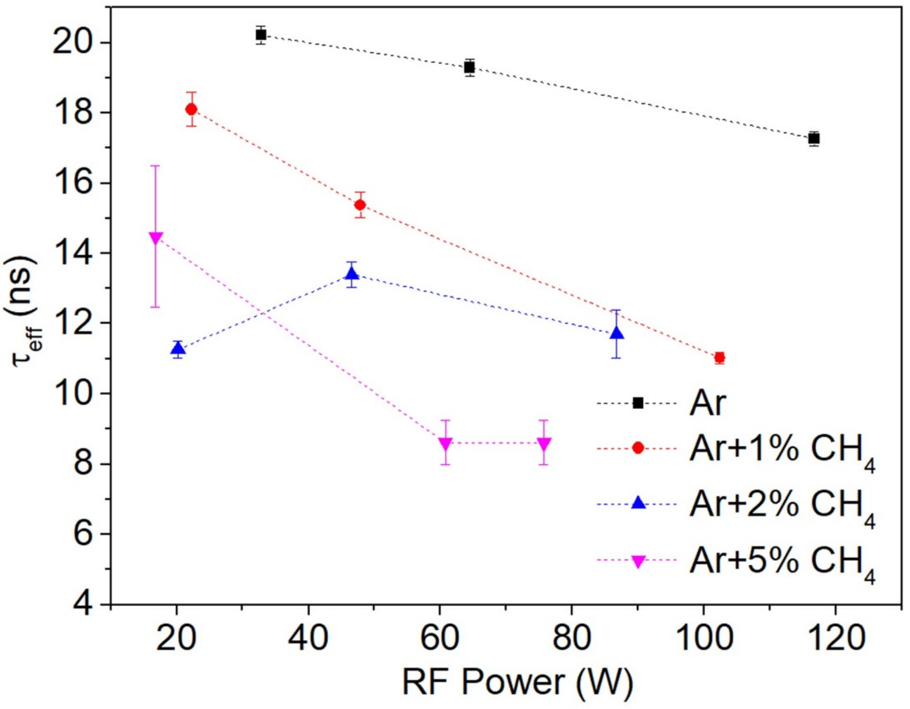

Figure 2. Effective fluorescence lifetime from the $2p_2$ level for varying gas and measured power conditions.

state populations. By measuring the intensity of the Rayleigh signal, an absolute instrumental factor was determined, which accounts for the collection solid angle, optical transmission, and detector quantum efficiency. To relate the calibrated fluorescence signal to the initial Ar $1s_5$ density, a time-dependent, 5-level population dynamics model was employed. This model simulates the evolution of the relevant Ar energy levels during and after the nanosecond laser pulse, considering laser-induced excitation and de-excitation, spontaneous radiative decay, and collisional quenching processes. By solving a system of rate equations, the model calculates the fraction of the initial metastable population that is transferred to the fluorescing $2p_2$ level and subsequently decays through the observed channel. The absolute density of the Ar $1s_5$ state was then determined by combining the population of the fluorescing level, the measured LIF signal, and the calibrated instrumental factor. Here, we must note that fluorescence decay time varies with power and gas composition, and therefore, it must be determined for optimal conversion of the LIF signal to density. The measured effective fluorescence lifetimes are plotted vs power for all considered gas compositions at figure 2. Gas temperature was measured via Swan band emission [52] and is detailed in a separate study [51].

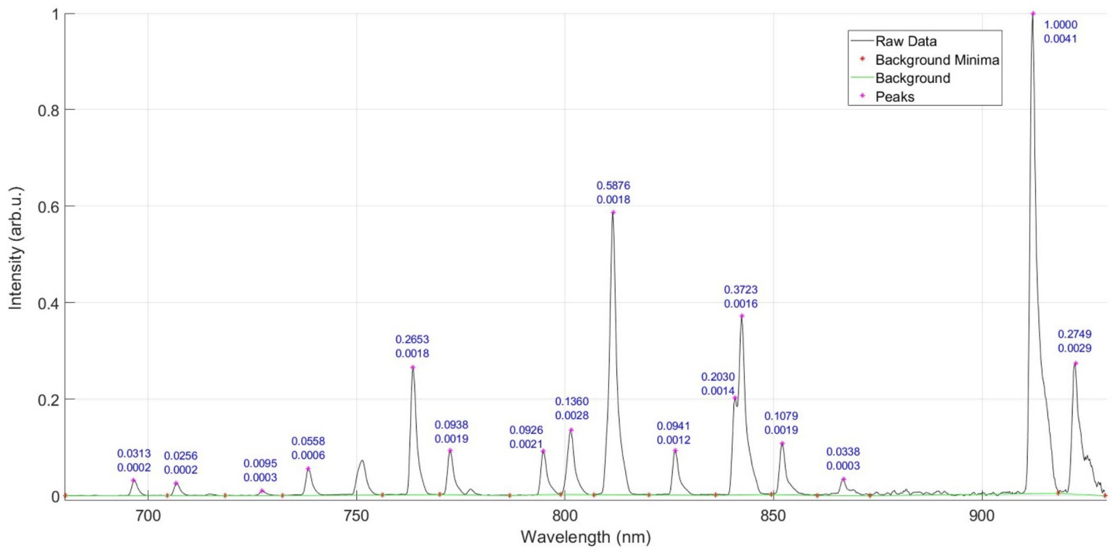

Figure 3. Broadband spectrum example with the determined background and normalized intensities.

The LIF images were corrected for background, as the signal collected with the optical filter includes the LIF, plasma emission from $2p_2$ level, and contributions from laser scattering in the chamber. The background image was collected immediately following the signal collection, after detuning the laser away from the $1s_5$–$2p_2$ transition by 0.73 nm. The resulting image is also useful for inspecting the plasma shape.

2.3. Broadband spectroscopy

The broadband spectra were acquired with a broadband spectrometer (Ocean Optics 4400+ HR), with a coupled optical fiber on a 2-axis positioner. The plasma image was translated with a 2″ aspheric lens ($f = 40$ mm). In the image plane, the optical fiber aperture is positioned at the location of the peak of the LIF signal. For each condition, we collected 100 spectra with an exposure time of 5 ms. The collected spectra were corrected for optics transmission and spectrometer response function by using a calibrated tungsten-halogen light source (SL1-cal, StellarNet).

2.3.1. Spectral feature extraction

Spectrum processing included finding the peaks and their intensities for the emission from the Ar I 2p levels. To analyze the spectra, we used MATLAB's findpeaks function with a prominence threshold of 0.5% of the maximum intensity to detect the peaks for the emission from Ar1 2p levels. We have tracked the intensity of 16 Ar emission lines (696.54, 706.72, 727.3, 738.4, 763.51, 772.42, 794.82, 801.47, 811.53, 826.45, 840.82, 842.46, 852.14, 866.8, 912.29, and 922.45 nm) with corresponding upper energy levels (ranging from 12.9 to 13.32 eV). We should note that in pure Ar plasma, the emission spectra feature measurable lines in the 415–420 nm range. These lines originate from excited 1s levels with energies ∼14.5 eV and therefore are valuable spectral features. We have used them reliably as additional features for training and predictions in pure Ar plasma. In the Ar + CH_4 plasma, this region features a strong CH(C–X) band, and the Ar lines could not be discerned. We also skipped Ar emission from 2p levels at 750.39 and 751.46 nm in the analysis. The poor resolution of the broadband spectrometer did not allow a precise determination of the separate emission intensities from these two levels with a simplistic algorithm. It was also noticed that the ratio of these line intensities changes, i.e. in pure Ar the 750.39 nm line is stronger, but the addition of methane corresponds to the enhancement of the 751.46 nm line, which becomes the stronger of the two.

Background subtraction was performed by identifying minima between consecutive peaks, rejecting outliers via interquartile range (IQR) filtering (1.5 × IQR threshold) within inter-peak regions and median absolute deviation (MAD) across all minima (3 × scaled MAD threshold). The background was interpolated linearly across the full wavelength range and subtracted from peak intensities. This yielded a spectrum of baseline-corrected intensities for the reference lines (figure 3).

3. Results

3.1. Dynamics of Ar $1s_5$ density

This section reports the results of pLIF measurements of Ar $1s_5$ density. Figure 4 shows the plasma emission and Ar $1s_5$ density for a few representative conditions. For all studied conditions, the average densities of Ar $1s_5$ metastables and plasma emission (at 730 nm) are shown in figures 5(a) and (b), respectively. The measured Ar $1s_5$ densities vary in the range of $\sim 10^{16}$–10^{17} m^{-3}.

General behavior can be described as follows. In the pure Ar case, the plasma exhibits a clear structure of moving striations [54]. The striations are described in a separate study [51]. In pure Ar discharge, the spatial distribution and the density of Ar $1s_5$ do not change appreciably with power **in range 32.8–116.7 W.** With the addition of 1% methane, plasma-and, consequently, the distribution of Ar metastables-undergoes drastic changes (see figures 4(b) and (c)). At powers $P = 22$, 48 W, the emission appears diffused with the brightest region next to the ground electrode. The metastable density increases twofold, but its spatial distribution does not change compared to pure Ar (see figures 4(a) and (b)). At higher input powers the discharge contracts to filament [51], see for example figure 4(d), Ar + 1%CH_4, $P = 102$ W. The metastable distribution reflects the filamentation, and the density decreases (figure 5(a)).

For 2% and 5% $CH_{4,}$ the dynamics are similar: at measured $P \leqslant 47$ W and $P \leqslant 61$ W, respectively, the plasma is diffuse, and filamentation is observed at $P = 87$ and $P = 76$ W, respectively. The plasma emission at $P = 20$ W (2%CH_4) and $P = 17$ W (5% CH_4) is weak (figure 5(b)) and the Ar $1s_5$ density is reduced by an order of magnitude, compared to the pure Ar case. As power increases, the metastable density increases, likely due to an increase in plasma density, as predicted by a global balance model.

The non-linear increase in light intensity observed at high power across Ar–CH_4 mixtures (figure 5(b)) is directly correlated with the plasma transitioning from the diffuse to a contracted filamentary mode (figure 4(c)). We hypothesize that inside the filaments, the concentrated power rapidly increases the local electron energy and density, enhancing the stepwise excitation of Ar atoms to the radiating 2p levels. This phenomenon is a key indicator of the changing plasma regime and explains the sharp rise in emission intensity observed at the onset of filamentation for the different CH_4 admixtures.

3.2. Electron temperature measurement using an Ar I 763.51/811.53-line ratio

The Ar I 763.5/811.5 nm line intensity ratio has been used extensively to estimate electron temperature (T_e) in Ar plasmas [55–58]. The corona model, also known as the corona equilibrium model [59], is a simplifying assumption in plasma spectroscopy, typically suitable for low-pressure (typically <10–20 Pa) RF plasmas because the low electron density (n_e) ensures that radiative processes dominate over collisional ones, enabling straightforward estimation of electron temperature (T_e) from optical emission line ratios without the need for more complex CRMs. At higher pressures (including the pressure used in these studies, 2.6 Torr), the model's validity may be limited as metastable-atom contributions and radiation trapping become significant, but it can still offer approximate T_e values for diagnostic purposes in argon plasmas [60].

The fundamental balance equation for the density of an excited state (e.g. Ar 2p levels) in the corona model is:

$$n_{2p} = n_{gs} \cdot Q_{gs \rightarrow 2p} \cdot n_e \cdot \tau_{2p} \tag{1}$$

where n_{gs} is the ground-state atom density, $Q_{gs \rightarrow 2p}$ is the electron-impact excitation rate coefficient, n_e is the electron density, and $\tau_{2p} = 1/\Sigma A_{2p \rightarrow i}$ is the radiative lifetime (with $\Sigma A_{2p \rightarrow i}$ as Einstein coefficients for transitions to lower states i) [60]. The intensity ratio R for two emission lines (e.g. higher-energy line 'h' at 763.5 nm and lower-energy line 'l' at 811.5 nm) is then:

$$R = \frac{I_h}{I_l} = \frac{A_h \cdot \tau_h \cdot Q_h}{A_h \cdot \tau_h \cdot Q_h}. \tag{2}$$

This ratio is generally calculated by assuming a Maxwellian EEDF incorporated into the rate coefficients Q. For practical T_e estimation with close-energy Ar lines like 763.5/811.5 nm, a simplified form is [57–59]:

$$T_e = \frac{\delta}{\ln (R \cdot C)} \tag{3}$$

where $\delta = E_h – E_l$ is the energy difference of the upper levels of the two respective lines, $R = I_{763}/I_{811}$, and C is an empirical constant that accounts for differences in excitation pre-factors (including Einstein

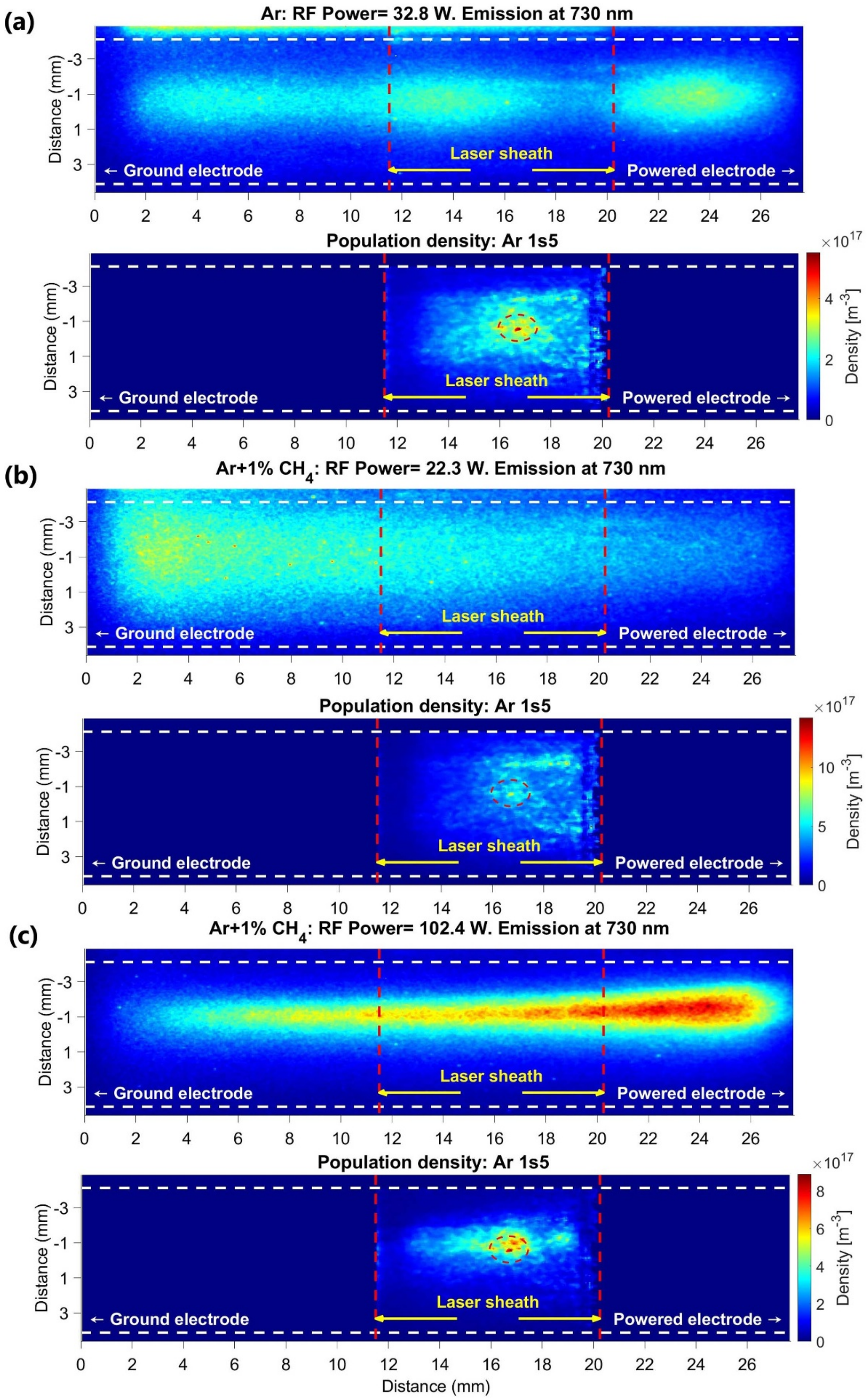

Figure 4. Plasma emission and Ar 1s$_5$ density for (a) Ar gas, P = 32.8 W (b) Ar + 1% CH$_4$, P = 22.3 W (c) Ar + 1% CH$_4$, P = 102.4 W.

A-coefficients and level degeneracies), branching ratios, and wavelength dependencies. Since the line intensities are in arbitrary units, the explicit wavelength correction is not always included, and *C* effectively absorbs those factors. The coefficients, including Einstein *A* values (e.g. $A_{763.5} = 2.45 \times 10^7$ s^{-1}, $A_{811.5} = 3.31 \times 10^7$ s^{-1}) and lifetimes τ, are sourced from the NIST atomic spectra database [61]; excitation cross sections σ (in 10^{-18} cm^2, e.g. $\sigma_{763.5,\mathrm{max}} \approx 3.2$, $\sigma_{811.5,\mathrm{max}} \approx 3$) are from experimental

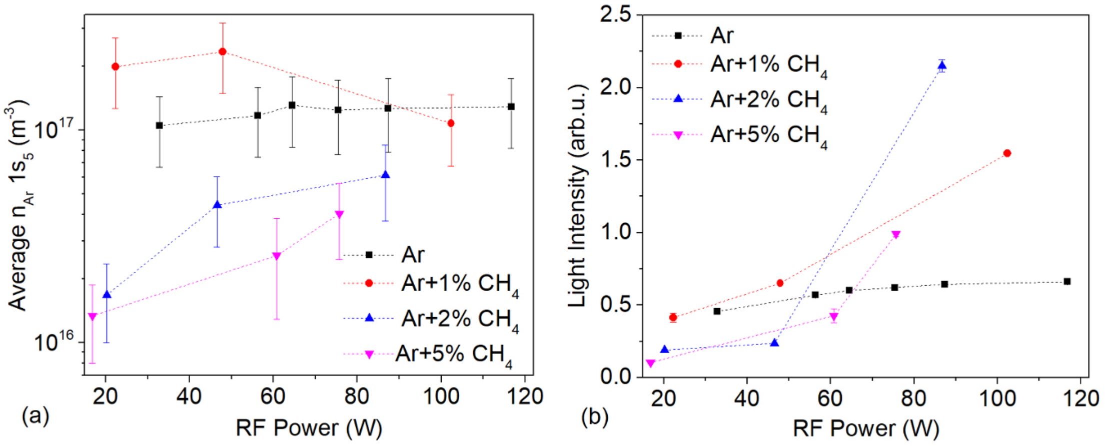

Figure 5. (a) Average density of Ar $1s_5$ in the area illuminated by the laser (b) plasma emission at 730 nm.

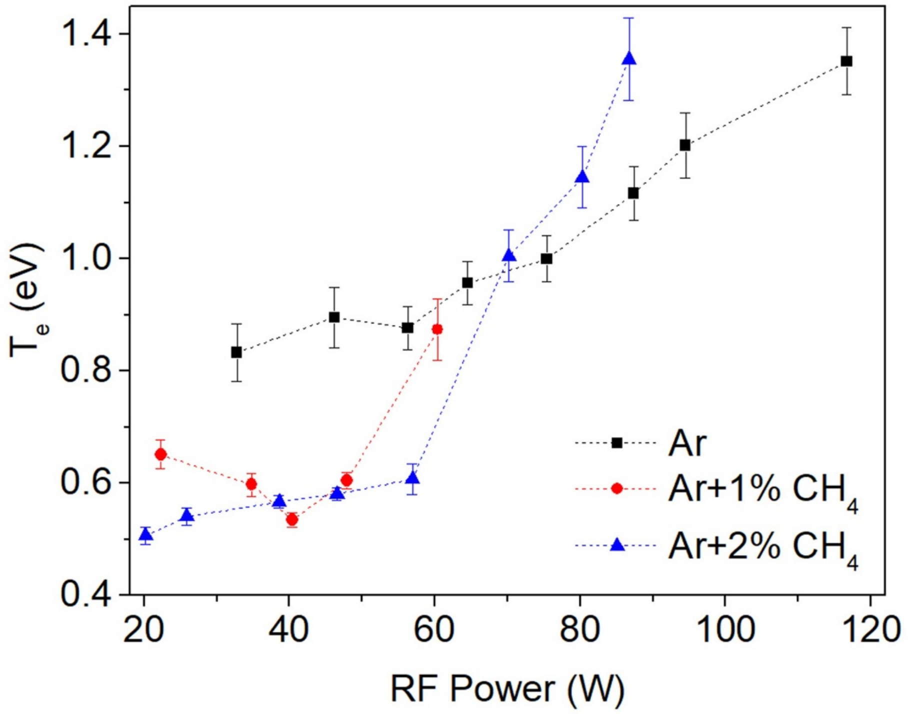

Figure 6. Electron temperature vs measured RF Power.

measurements by Boffard *et al* [62], which allows the derivation or fitting of C by approximating the rate coefficients Q in the full corona calculation.

The line intensities were extracted from each of the 100 spectra per gas/power condition. The mean value from the 100 spectra was used, with the standard deviation propagated to the error calculation. The resulting T_e as a function of the measured RF power is shown in figure 6. The data exhibit a two-regime behavior across all conditions: T_e remains relatively constant, ranging from approximately 0.8–1.0 eV for pure Ar and 0.5–0.8 eV for Ar–CH_4 mixtures, within error bars, over the measured power range of ~20–60 W. Above ~60 W, T_e increases sharply, reaching values between 1.1 and 1.4 eV at higher powers (up to ~120 W), with T_e for mixtures becoming equal to or exceeding that of pure Ar. Contraction of the plasma channel plays a major role in this heating for Ar/CH_4 mixtures, due to the increased energy density [51, 52]. The discussion of T_e dynamics is given in section 4.2.

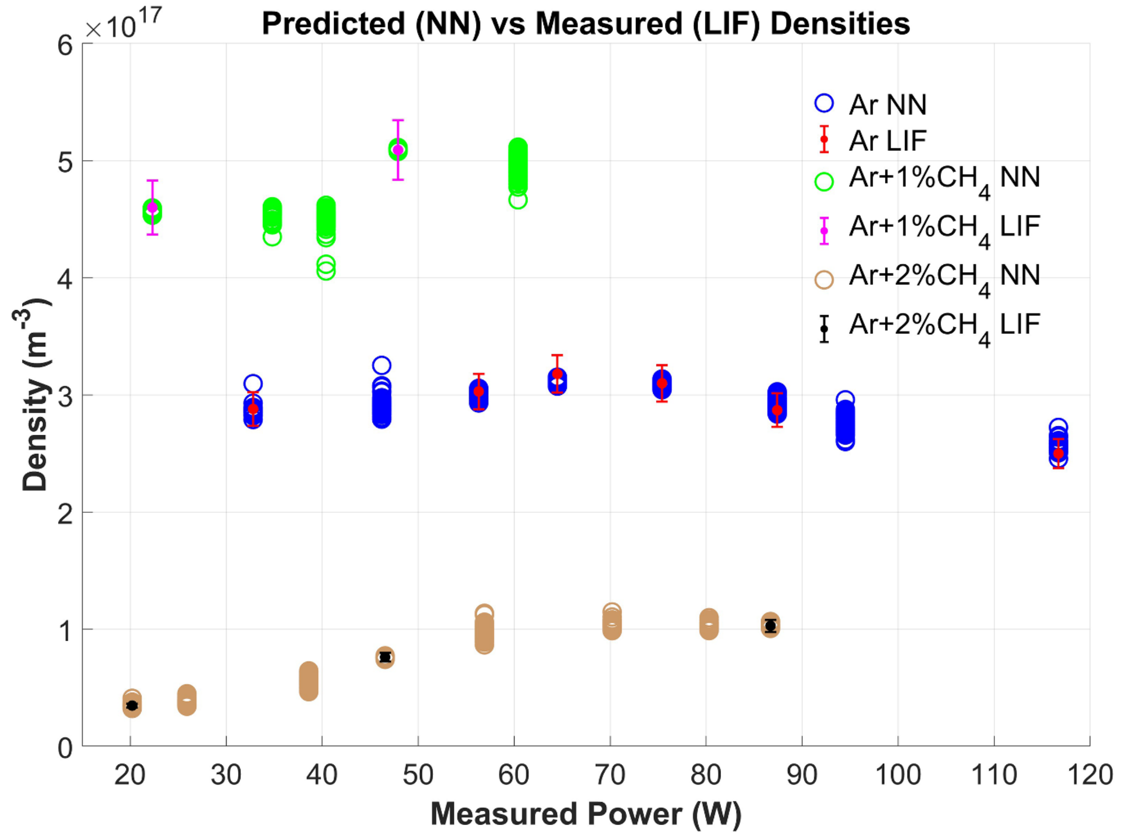

Figure 7. Measured 'local' Ar $1s_5$ densities versus densities predicted from individual broadband spectra. The Ar $1s_5$ densities used for training are averaged over the area observed by the spectrometer, indicated by a black dashed circle on the images in figure 4.

3.3. NN-based prediction of argon metastable ($1s_5$) density from optical emission spectra

To predict the density of argon atoms in the $1s_5$ metastable state (Ar $1s_5$) from OES data in argon (Ar) and argon–methane (Ar + CH_4) mixtures, we developed a NN model trained on extracted spectral features (line intensities). A NN, while powerful, can be a 'black box'; therefore, verifying that its inputs (emission intensities from the Ar 2p manifold) are fundamentally linked to its target output (the Ar $1s_5$ density) is critical to validate the approach beyond purely statistical fitting. We have conducted an analysis aimed to demonstrate that, under the conditions of this study, the population of the Ar 2p levels and thus their optical emission is primarily driven by stepwise electron-impact excitation from the Ar $1s_5$ metastable state rather than direct excitation from the ground state. This primary excitation pathway justifies using the Ar 2p emission features as reliable input parameters for the ML model that predicts the underlying metastable density. Full details and justification are provided in appendix B

Our approach involves processing raw spectra, extracting key Ar emission lines, normalizing features, and using a feedforward NN to regress Ar $1s_5$ density values and associated measurement uncertainties. This method was implemented in MATLAB, employing custom feature extraction and training scripts. The NN is trained on the 'local' density of Ar $1s_5$, obtained by averaging the data from a small area observed by the spectrometer (highlighted on figure 4 by a dashed black circle). The local density values are higher than the 'average' density values and are shown in figure 7(a).

3.4. Data preparation and training

Training data comprised OES spectra from three gas compositions = pure Ar, Ar + 1% CH_4, and Ar + 2% CH_4-collected at RF powers of 16–117 W (specific powers per gas: Ar at 33, 56, 64, 75, 87, 117 W; Ar + 1% CH_4 at 22, 48 W; Ar + 2% CH_4 at 20, 47, 87 W). One hundred spectra per condition were processed to augment the dataset.

A unified set of reference wavelengths was compiled by pooling unique detected lines across all training spectra, resulting in a fixed feature dimension (16 lines) in the spectral range of 680–930 nm. A procedure for outlier filtering was engaged, but no outliers were found in the collected data. Targets were the 'local' Ar $1s_5$ densities (m^{-3}) and errors from LIF measurements.

The dataset yielded an input matrix X (features × samples) and target matrix T (2 × samples: density and error). Features were z-score normalized globally. Targets were min-max normalized to $[-1, 1]$. A feedforward NN was trained using MATLAB's fitnet with hidden layers and Levenberg–Marquardt optimization (trainlm). Training parameters included 500 epochs, early stopping, 0.005 regularization, and data splits (70% train, 15% validation, 15% test). We have examined various NN architectures, and the results are shown in table A1. Performance was evaluated via mean squared error (MSE) on normalized outputs, R^2, and mean absolute percentage error (MAPE) on density predictions. The R^2 value indicates how well the NN's predictions explain the variance in the data—values close to 1 mean it is capturing most of the patterns, while 0 or negative values suggest that performance is not better than guessing the average. The MAPE value shows the average percentage difference between predicted and actual values, with a lower value indicating higher relative accuracy. The MSE value averages the squared differences between predictions and actual values, assigning higher penalties to large deviations. Lower MSE values indicated a tighter fit. ValPerf is a metric of loss on the validation set, reflecting how the NN generalizes unseen data. Lower ValPerf is better, as it means less error on unseen data. Together, they gauge the NN's fit (R^2), error scale (MSE/MAPE), and robustness (ValPerf).

We optimized the NN architecture by varying hidden layers (1–4), neurons per layer (10–80), regularization (0.001–0.01), and epochs (100–500). Results reveal a clear trend toward improved performance with increasing model complexity, up to an optimal point beyond which overfitting occurs. Single-layer networks with 10–80 nodes yield high R^2 values (0.996–0.997) but moderate errors (MAPE 3.6–5.0%, MSE ∼0.001), with validation performance ranging from 0.000 87 to 0.0028, peaking at the 40-node architecture. Two-layer models significantly enhance accuracy ($R^2 \geqslant 0.999$, MAPE $< 2.1\%$, MSE < 0.0004), achieving a ValPerf as low as 0.000 44 for [40 20] and [80 40]. Three-layer configurations further refine results, with [50 30 15] delivering the lowest ValPerf among them at 0.000 34. Four-layer architectures culminate in the overall best performer, [80 40 20 10] (R^2 0.9998, MAPE 0.74%, MSE 0.00014, ValPerf 0.000 26), but larger variants like [200 100 50 25] show degraded ValPerf (0.0017), indicating overfitting. The [80 40 20 10] architecture was chosen as optimal, balancing superior fit and generalization without excessive complexity.

Full results for all probed architectures are summarized in table A1 in appendix C.

3.5. NN-based prediction of Ar 1s5 density

For prediction, multiple individual spectra for each condition were processed similarly to the training spectra: loaded, features extracted and normalized, then fed to the NN. Outputs were reverse normalized to obtain Ar $1s_5$ density and error estimates. Predictions were performed for extended power levels (applied powers: 50, 65, 80, 100, 120, 150, 175, and 200 W, measured powers vary per gas composition, see table 1) for each of the 100 spectra captured per condition. Feature extraction identified 16 consistent Ar emission lines across all spectra. The results are shown in figure 7. The predicted values for each of the 100 spectra per condition are shown as individual markers. The comparison of predicted and measured densities illustrates the efficacy of the NN in replicating measured Ar $1s_5$ metastable densities across varying power levels and gas admixtures, underscoring its capacity for accurate trend capture. The spread of predictions is tight on trained conditions, which means the NN is confident there—it is interpolating from familiar data, with low uncertainty. In untrained conditions, wider spread is evident- the NN is extrapolating and guessing.

3.6. Feature importance analysis

A permutation feature importance analysis was performed to determine the contribution of individual Ar I lines to the neural-network prediction of the Ar $1s_5$ metastable density (figure 8). The method repeatedly shuffles one input feature across all spectra and measures the resulting increase in prediction error; larger increases indicate higher importance.

The results show a strong concentration of predictive power: the four most important lines—763.51 nm (30.7%), 801.47 nm (17.5%), 811.53 nm (12.5%), and 738.40 nm (10.1%) together account for approximately 70% of the total importance. The 763.51 nm line ($2p_6 \rightarrow 1s_5$), despite its modest raw intensity, dominates because of its high excitation threshold from the metastable level (∼1.95 eV above $1s_5$). Its emission intensity is therefore particularly sensitive to both the metastable density and the high-energy tail of the EEDF.

To test whether this importance ranking translates into practical simplification, new networks of identical architecture were retrained using only the N highest-ranked lines. Their predictive accuracy was then evaluated on previously unseen plasmas, i.e. on the full set of broadband OES spectra acquired at power levels and gas mixtures that were deliberately excluded from the training dataset (the same independent test set used for figure 7). This ensures a rigorous, real-world assessment of generalization

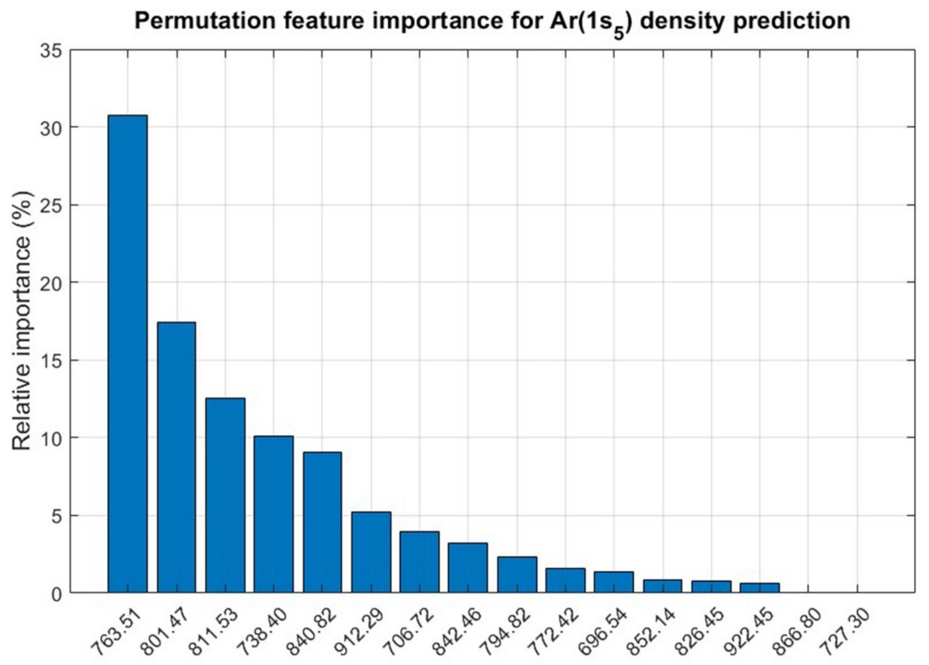

Figure 8. Permutation feature importance of the 16 Ar I lines. The top five lines carry ~78% of the total predictive information.

Table 2. Performance of simplified models on 'unseen' plasmas.

Number of lines used	'Most important lines' included	MAE ($\times 10^{15}$ m^{-3})	Relative to the full model
1	763.51 nm	50	1490%
3	763.51, 801.47, 811.53 nm	4	119%
5	+738.40, 840.82 nm	3.53	105%
8	+912.29, 706.72, 842.46 nm	3.8	113%
16 (full)	All	3.37	100%

Table 3. Dominant rates (order-of-magnitude) in the different operating regimes.

Regime	CH_4 fraction	Dominant production of Ar $1s_5$	Dominant loss of Ar $1s_5$	Net effect on Ar $1s_5$ density
Diffuse $n_e \approx 10^{15}$–10^{16} m^{-3}	0%	e^- + Ar(ground) → higher levels → cascade	Stepwise ionization + superelastic collisions ($k \sim 10^{-15}$–10^{-14} $m^3 s^{-1}$) [23]	≈ Constant with power
Diffuse $n_e \approx 10^{15}$–10^{16} m^{-3}	≈1%	e^- + Ar(ground) → higher levels → cascade	Same loss processes, but reduced T_e → slower loss	↑ (Factor ≈ 2)
Diffuse $n_e \approx 10^{15}$–10^{16} m^{-3}	⩾2%	e^- + Ar(ground) → higher levels → cascade	Penning quenching by CH_4 ($k \approx 4.16 \times 10^{-16}$ m^3 s^{-1}) [63]	↓↓ (order of magnitude)
Filamentary (high-power) $n_e > 10^{16}$ m^{-3}	1%–5%	High local n_e, T_e. Enhanced direct excitation (from ground) + cascade.	Penning quenching (CH_4) [63] + enhanced stepwise excitation ($1s_5 \rightarrow 2p$)/ionization and superelastic collisions [23]	Stagnates or decreases with power

performance rather than overfitting to the training conditions. Performance is quantified by the mean absolute error (MAE)—the average absolute deviation between the neural-network prediction and the LIF-measured Ar $1s_5$ density—in units of m^{-3}. The results are summarized in table 2.

A dramatically simplified model using only the five most important lines retains more than 95% of the full-model accuracy on these unseen plasmas (MAE = 3.53×10^{15} m^{-3} versus 3.37×10^{15} m^{-3} for the full 16-line model). This demonstrates that the NN successfully distills the broadband spectrum into a compact, physically meaningful subset of diagnostic lines, paving the way for real-time metastable monitoring with greatly reduced optical and data-processing complexity.

4. Discussion

4.1. Physical mechanisms governing the non-monotonic Ar($1s_5$) density

The central experimental observation of this work is the non-monotonic dependence of the Ar $1s_5$ metastable density on CH_4 admixture: a moderate increase at ≈1% CH_4 and a strong depletion (by roughly an order of magnitude) at ⩾2% CH_4. A qualitative picture that is consistent with the measured data and literature rate coefficients is presented in table 3 (dominant production and loss channels in each regime). Production of Ar $1s_5$ in the diffuse mode is dominated by electron-impact excitation from the ground state, followed by radiative cascade into the 1s manifold; only the loss balance changes with CH_4 fraction and plasma mode.

In the diffuse mode ($P \leqslant 60$ W), electron temperature remains low (0.5–1 eV) and relatively independent of power. Adding a small amount of CH_4 (≈1%) cools the electrons via vibrational excitation of methane (see appendix A). It thereby reduces the rates of energy-loss processes that deplete metastables (stepwise ionization and superelastic collisions, both of which scale steeply with T_e). The additional quenching by CH_4 itself is still weak at 1%, so the net metastable density rises. At CH_4 fractions ⩾2%, the direct Penning-type quenching channel Ar $1s_5 + CH_4 \rightarrow$ products (rate coefficient $\approx 4.16 \times 10^{-16}$ m^3 s^{-1}) [63] dominates and rapidly depletes the metastable population despite the continued presence of the other production pathways.

At higher power, the plasma contracts into bright filaments [51], marking a transition from the diffuse mode to a contracted regime driven by enhanced power deposition and spatial non-uniformities [64]. Inside these filaments, the local electron density and temperature increase significantly ($n_e > 10^{16}$ m^{-3}, $T_e \approx 1.1$–1.4 eV), due to ambipolar electric fields during sheath expansion and nonlocal electron heating, leading to anisotropic EEDFs with pronounced high-energy tails [65]. Production of Ar $1s_5$ is boosted by direct electron-impact excitation from the ground state (threshold ∼11.55 eV), but stepwise excitation from Ar $1s_5$ to radiating 2p levels is strongly enhanced by the high local n_e and T_e, which is why the 730 nm emission intensity rises sharply (figure 5(b)). However, the same high-density, higher T_e environment also intensifies metastable loss via stepwise ionization (Ar $1s_5 + e^- \rightarrow Ar^+ + 2e^-$, threshold ∼4.2 eV from $1s_5$) and superelastic collisions, whose rates scale more steeply with T_e due to lower thresholds. Because the quenching rate by CH_4 is already close to gas-kinetic at ⩾2% ($k = 4.16 \times 10^{-16}$ m^3 s^{-1}) [63], and filaments may locally concentrate precursors via transport gradients, the loss channels again dominate, and the metastable density either stagnates or decreases with further power increase.

Thus, the non-monotonic behavior and the differing power dependences in the diffuse and filamentary regimes arise from the competition between a small number of well-characterized processes whose relative strengths shift dramatically with only a few percent of molecular admixture and with the onset of filamentation. A quantitative global or 2D kinetic model would be required to reproduce the data exactly, but the qualitative picture above is fully consistent with the present measurements and with literature rate coefficients.

The radiative lifetime of Ar $1s_5$ in vacuum is ∼38 s [66]. In our 2.6 Torr discharge, collisional processes dominate. In low-pressure plasmas, a major mechanism of metastable loss is electron-impact superelastic de-excitation and excitation to higher levels, with literature citing a rate constant ~ 2–5×10^{-13} m^3 s^{-1} in low-pressure argon positive column ($T_e < 2$ eV) [62, 67]. In pure argon, electron-impact excitation and stepwise ionization from the $1s_5$ state have rate coefficients ≈ 0.1–1×10^{-13} m^3 s^{-1} at $T_e \approx 0.5$–1.4 eV. The rates are estimated by integrating the cross-sections [67, 68] over a Maxwellian EEDFat electron densities $n_e \approx 10^{15}$–10^{16} m^{-3} [64, 65]. This estimation yields an effective lifetime of ∼0.2 ms–5 ms. Adding ⩾2% CH_4 introduces fast Penning quenching ($k = 4.16 \times 10^{-16}$ m^3 s^{-1}) [63]. At the measured gas temperature $T_g \approx 1200$ K[51], $n_{CH_4} \approx 4.2 \times 10^{20}$ m^{-3}, reducing the effective lifetime to ∼10–50 μs. These short lifetimes underscore the sensitivity of the metastable population to small gas admixtures and are relevant for reactor design, as they set the timescale for metastable-driven chemistry and diffusion.

4.2. Electron temperature trends

The electron temperature figure 6, derived from the Ar I 763.51/811.53 nm line ratio in the corona approximation, exhibits two distinct regimes: a low-power plateau ($T_e \approx 0.8$–1 eV in pure Ar, 0.5–0.8 eV with CH_4) and a sharp rise above ≈60 W in the filamentary regime. The systematic reduction of T_e upon CH_4 addition is caused by efficient vibrational cooling of electrons (appendix A); at 1% CH_4, the vibrational loss rate exceeds elastic cooling by argon by more than an order of magnitude at $T_e \approx 0.8$ eV. The rise of T_e at high power reflects the increased heating efficiency in the contracted, resistive filamentary mode [51, 52].

4.3. Neural-network-augmented broadband OES

The trained feed-forward NN accurately reproduces both absolute Ar 1s$_5$ densities and their dynamic trends from the intensities of 16 Ar I lines (figure 7). Because stepwise excitation from the metastable level dominates the population of the radiating 2p manifold under the present conditions (appendix B), the emission intensities carry direct information about the underlying metastable density, providing a sound physical basis for the data-driven mapping.

4.4. Implications for plasma-assisted materials synthesis

The extreme sensitivity of Ar 1s$_5$ density to percent-level molecular admixtures demonstrated here explains why small changes in precursor flow or reactor contamination can dramatically alter growth rates and material properties in argon-based nanoparticle and thin-film syntheses. The NN-augmented OES diagnostic offers a simple, real-time monitor of this critical hidden parameter, paving the way for active feedback control in industrial-scale flow-through reactors.

4.5. Transferability and limitations of the NN-augmented OES

One of the objectives of this work is to demonstrate the principle of using a NN augmented with OES to create a simple, real-time 'sensor' that can track the Ar 1s$_5$ metastable density. The success of this approach is founded on the core physical finding that stepwise excitation from Ar 1s$_5$ is the dominant mechanism for populating the radiating 2p levels in our plasma (as demonstrated in appendix B).

Furthermore, the Permutation Feature Importance Analysis (section 3.6) strongly supports this principle by showing that the NN relies heavily on lines 763.51 nm, 801.47 nm, etc, known to be sensitive to this low-energy, stepwise excitation channel, confirming the model is learning the correct underlying physics. This capability is particularly valuable for commercial processing reactors where access for LIF is often impossible during routine operation, as the NN enables a simple, continuous, and cost-effective sensor for real-time monitoring of this critical parameter, facilitating closed-loop process control and optimization.

The NN model can be adapted to different plasma setups by retraining on site-specific LIF/TDLAS or equivalent calibration data, potentially extending to similar Ar-based chemistries in other reactors, such as those for SiC synthesis or etching processes. For reasonably similar plasmas (e.g. comparable pressures, powers, and Ar-rich mixtures), direct application may be feasible after calibrating for transmission and instrument response, allowing the NN to interpret line intensity sets within its trained range as proxies for Ar 1s$_5$ densities, provided stepwise excitation dominance holds.

However, challenges and limits must be acknowledged, underscoring that the current model is not universal but a demonstration of principle:

(i) Reliance on stepwise excitation dominance in Ar-rich plasmas at moderate pressures ($\sim$2–3 Torr), with poor generalization to highly diluted or non-Ar dominant gases.
(ii) Sensitivity to deviations in EEDF or other parameters not captured in training, which could require additional features or retraining.
(iii) At pressures much higher than 2.6 Torr, increased radiation trapping and quenching may alter emission dynamics, reducing accuracy without recalibration.
(iv) Performance is tied to training data quality and range, so extrapolation beyond tested conditions (e.g. $>$5 CH_4 or unfamiliar intensity patterns) introduces uncertainty, as seen in wider prediction spreads for untrained cases.

Future efforts could broaden the model scope to include other plasma parameters (like electron density and temperature, with accompanying measurements thereof or kinetic modeling) and integrate it into closed-loop control systems for enhanced plasma monitoring.

5. Conclusions

This study reveals a non-monotonic response of Ar 1s$_5$ metastable densities to CH_4 admixture in sub-atmospheric RF CCP, with enhancement at 1% and depletion at $\geqslant$2%, alongside a plateau in T_e below 60 W and rise above, modulated by gas composition. This ability to precisely modulate the density of key energy carriers via small gas admixtures is critically important for applications like plasma-assisted synthesis, where Ar metastables can drive the dissociation of molecular precursors and influence the growth and properties of nanomaterials. The NN-augmented OES diagnostic, trained on LIF data, enables accurate, real-time metastable tracking from spectral features, offering a cost-effective, non-invasive alternative to traditional methods for industrial monitoring. While the NN model is readily transferable to similar Ar-rich plasma setups through recalibration, its current applicability focuses on stepwise-dominant conditions at moderate pressures, with potential for broader use via expanded training data. Future efforts could extend the NN to additional parameters like n_e and T_e, for broader monitoring of the plasma facilitated by N_e/T_e measurements or modeling. The permutation feature-importance analysis shows that >70% of the NN's predictive skill is carried by only four Ar I lines, with the 763.51 nm transition ($2p_6 \rightarrow 1s_5$) alone contributing ~31%. This confirms that the trained model genuinely extracts information about the hidden metastable population rather than overfitting to noise or unrelated spectral features. More importantly, retrained networks using only the top three to five lines achieve >95% of the full model's accuracy on unseen data. Thus, real-time monitoring of Ar $1s_5$ density in industrial Ar-rich reactors can be reduced to measuring just a handful of carefully chosen emission lines.

Acknowledgments

This work is funded by the U.S. Department of Energy (DOE), Office of Fusion Energy Sciences under Contract No. DE-SC0021379, and the Office of Energy Efficiency and Renewable Energy (EERE) Contract DE-AC02-09CH11466.

The authors would like to thank Professor Yiguang Ju for the fruitful discussions that contributed to this work.

Data availability statement

The data that support the findings of this study are openly available at the following URL/DOI: https://doi.org/10.34770/3tw2-2k05 [75].

Author contributions

Shurik Yatom 0000-0001-8716-8487
Conceptualization (equal), Data curation (lead), Formal analysis (lead), Funding acquisition (supporting), Investigation (lead), Methodology (lead), Project administration (supporting), Resources (equal), Software (lead), Supervision (equal), Validation (equal), Visualization (lead), Writing – original draft (lead), Writing – review & editing (equal)

Sophia Gershman 0000-0002-8409-4029
Conceptualization (supporting), Data curation (supporting), Formal analysis (supporting), Funding acquisition (supporting), Investigation (supporting), Methodology (supporting), Project administration (supporting), Resources (equal), Software (supporting), Supervision (equal), Validation (supporting), Visualization (supporting), Writing – original draft (supporting), Writing – review & editing (equal)

Yevgeny Raitses 0000-0002-9382-9963
Conceptualization (equal), Data curation (supporting), Formal analysis (supporting), Funding acquisition (equal), Investigation (supporting), Methodology (supporting), Project administration (lead), Resources (equal), Software (supporting), Supervision (supporting), Validation (supporting), Visualization (supporting), Writing – original draft (supporting), Writing – review & editing (equal)

Appendix A

To quantify the relative importance of elastic and inelastic electron energy loss mechanisms in Ar–CH_4 plasmas, we calculated Maxwellian-averaged energy loss rates as a function of electron temperature. The calculations assume representative experimental conditions: total pressure of 2.6 Torr, argon ground-state density $n_{Ar} = 3.24 \times 10^{22}$ m^{-3}, methane density $n_{CH_4} = 2.1 \times 10^{20}$ m^{-3} (1% admixture), and electron density $n_e = 1 \times 10^{16}$ m^{-3}. While n_e scales the absolute magnitude of energy loss rates, it does not affect the relative importance of different collision channels.

Cross-section data
Energy-dependent electron-impact cross-sections were obtained from literature sources. For argon elastic scattering (momentum transfer), we used data from Bell *et al* [69] and Ferch *et al* [70], which

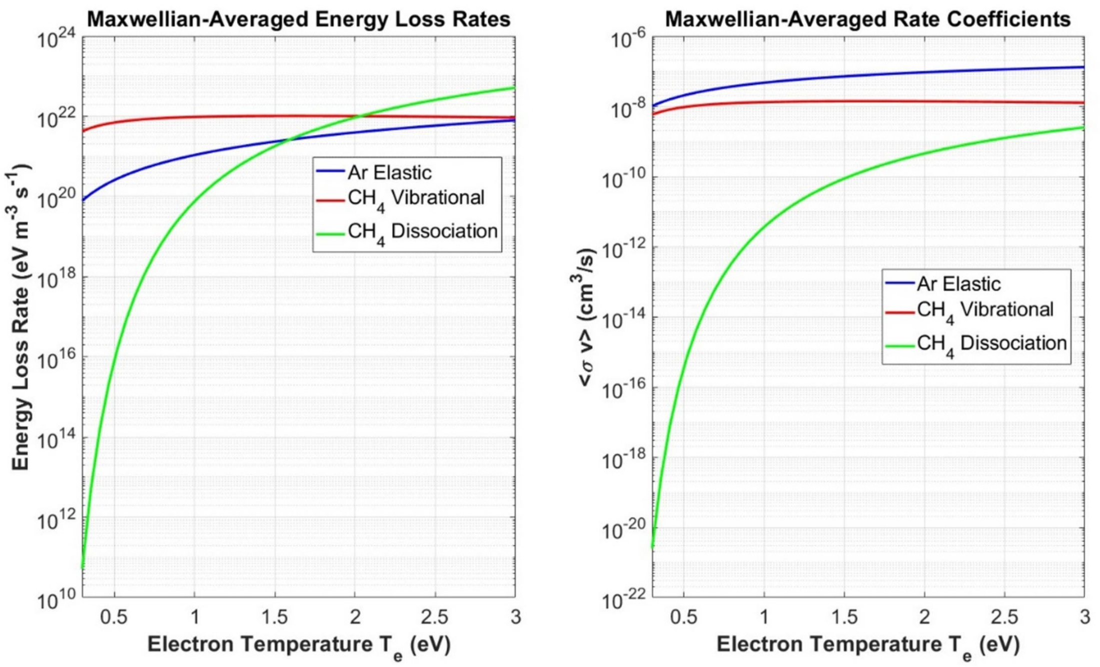

Figure A1. Comparison of elastic and inelastic energy loss mechanisms. (a) Maxwellian-averaged volumetric energy loss rates and (b) rate coefficients versus electron temperature for Ar–CH_4 plasma at 2.6 Torr with 1% CH_4. Inelastic vibrational excitation dominates total energy loss despite lower collision rates due to significantly higher energy removal per collision compared to elastic scattering.

capture the characteristic Ramsauer–Townsend minimum at ∼0.3 eV and the subsequent rise to ∼5–8 × 10^{-16} cm^2 at 1–10 eV. For methane, vibrational excitation cross-sections (summed over all modes) and dissociation cross-sections were taken from Song *et al* [71], with thresholds at 0.162 eV and 8.8 eV, respectively. Cross-section data were interpolated onto a fine energy grid (0.01–100 eV, 5000 points) using piecewise cubic Hermite interpolation.

Maxwellian electron energy distribution function (EEDF)

For each electron temperature T_e in the range 0.3–3.0 eV, we constructed a Maxwellian EEDF in energy space:

$$f(E) = \frac{2}{\sqrt{\pi}} \frac{\sqrt{E}}{T_e^{3/2}} e^{-\frac{E}{T_e}} \tag{A1}$$

normalized such that $\int_0^\infty f(E)\,dE = 1$. The electron velocity at each energy point is:

$$v(E) = \sqrt{\frac{2E \cdot q_e}{m_e}} \tag{A2}$$

Rate coefficient calculation

Maxwellian-averaged rate coefficients were computed by integrating over the EEDF:

$$\langle \sigma v \rangle = \int_0^\infty \sigma(E) \cdot v(E) \cdot f(E)\,dE \tag{A3}$$

where $\sigma(E)$ is the energy-dependent cross-section for each process (elastic, vibrational, or dissociation). Integration was performed numerically using the trapezoidal rule over the energy grid extending to 100 eV to capture the high-energy tail contributions.

Energy loss rate calculation

The volumetric energy loss rate (power density) for each process was calculated as:

$$P_{\text{loss}} = n_g \cdot n_g \cdot \langle \sigma v \rangle \cdot \langle \Delta E \rangle \tag{A4}$$

where n_g is the target gas density (n_{Ar} or n_{CH_4}) and $\langle \Delta E \rangle$ is the average energy lost per collision. For inelastic processes (vibrational excitation and dissociation), $\langle \Delta E \rangle$ is constant: 0.35 eV for vibrational excitation and 9.8 eV for dissociation. For elastic collisions, the energy loss per collision depends on the electron energy: $\Delta E_{\text{elastic}} = E \times (2m_e/M_{Ar})$, where the mass ratio $2m_e/M_{Ar} \approx 2.74 \times 10^{-5}$. The average elastic energy loss was computed as:

$$\langle E \cdot \delta \rangle = \int_0^\infty E \cdot \frac{2m_e}{M_{Ar}} \sigma_{\text{elastic}}(E) \cdot v(E) \cdot f(E)\,dE \tag{A5}$$

Results

Figure A1 a shows the calculated volumetric energy loss rates versus electron temperature. Despite CH_4 comprising only 1% of the gas mixture, vibrational excitation contributes energy loss rates comparable to or exceeding elastic scattering with argon across the experimental T_e range (0.5–1.4 eV). This occurs because inelastic collisions remove $\sim 10^4$ times more energy per collision than elastic collisions, compensating for both the lower CH_4 density ($\sim 150 \times$ less than Ar) and the somewhat lower collision rate coefficients. At $T_e = 0.8$ eV, for example, the CH_4 vibrational loss rate exceeds Ar elastic loss by a factor of ~ 13, explaining the observed electron cooling upon CH_4 addition. The right plot (figure A1(b)) shows the Maxwellian-averaged rate coefficients $\langle \sigma v \rangle$, demonstrating that while argon elastic collision rates are higher, the energy loss efficiency per collision determines the overall cooling dynamics.

Appendix B. Physical basis for neural network (NN)-augmented OES-linking Ar 2p emission to Ar 1s$_5$ density

Before employing a NN to predict Ar 1s$_5$ densities from OES spectra, it is essential to establish a physical basis for the correlation. A NN, while powerful, can be a ‘black box’; therefore, verifying that its inputs (emission intensities from the Ar 2p manifold) are fundamentally linked to its target output (the Ar 1s$_5$ density) is critical to validate the approach beyond purely statistical fitting. The following analysis aims to demonstrate that, under the conditions of this study, the population of the Ar 2p levels and thus their optical emission is primarily driven by stepwise electron-impact excitation from the Ar 1s$_5$ metastable state rather than direct excitation from the ground state. This primary excitation pathway justifies using the Ar 2p emission features as reliable input parameters for the ML model that predicts the underlying metastable density.

Let us consider a simplified picture of 3-level dynamics with the corresponding densities: n_g (ground level, 0 eV), n_m (1s$_5$ metastable level, 11.55 eV), and n_u (general 2p level, 12.9–13.5 eV), see figure A2.

Figure A2. (a) Simplified schematics of the considered 3-level system (b) normalized EEDF fractions for direct and stepwise excitation. A. The line emission from the 2p level is:

$$I_{ul} = n_u A_{uk} h\nu_l. \tag{A6}$$

Here,

$$n_u = \frac{n_e n_g \langle \sigma v \rangle_{g \to u} + n_e n_m \langle \sigma v \rangle_{m \to u}}{A_u} \tag{A7}$$

comprises direct (>12.9 eV) and stepwise (1.4–4.2 eV) excitation terms. A simple model computed the excitation rates for the Ar I 2p levels, considering direct excitation from the ground state and stepwise excitation via the metastable 1s$_5$ state. The EEDF was approximated as a Maxwellian, with T_e ranging from 0.5 to 10 eV. The excitation terms were calculated as:

$$R_{\text{direct}} = n_e \cdot n_g \cdot \langle \sigma v \rangle_{g \to u} \tag{A8}$$

$$R_{\text{stepwise}} = n_e \cdot n_m \cdot \langle \sigma v \rangle_{m \to u} \tag{A9}$$

where $n_e = 10^{15}$–10^{16} m^{-3} is the electron density, $n_g \sim 2.1 \cdot 10^{22}$, m^{-3} is the ground-state density, $n_m = 10^{16}$–5×10^{17} m^{-3} is the metastable density, and $<\sigma v>$ is the Maxwellian-averaged rate coefficient obtained by integrating $\sigma(E) \cdot v(E) \cdot F(E)$ over the energy range, with $\sigma(E)$ interpolated from experimental cross-sections [67]. The direct excitation energy threshold was set from 12.9 to 15.755 eV (below the ionization potential of 15.76 eV), while stepwise excitation spanned 1.4–4.21 eV, reflecting the lower

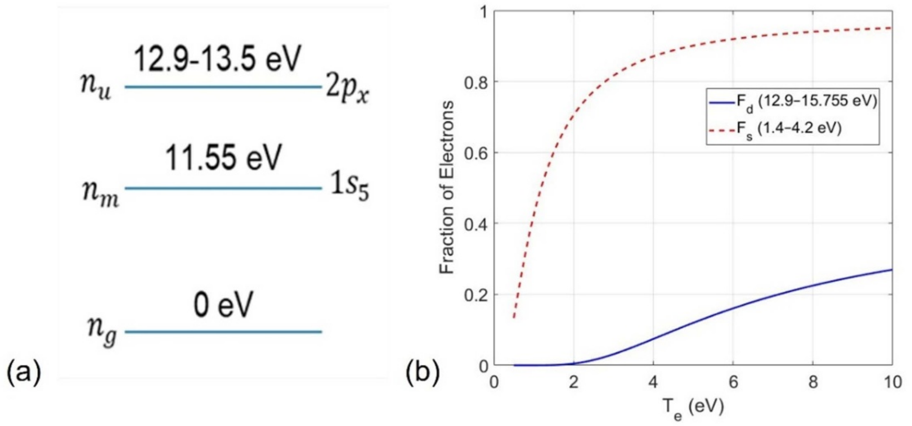

Figure A2. (a) Simplified schematics of the considered 3-level system (b) normalized EEDF fractions for direct and stepwise excitation.

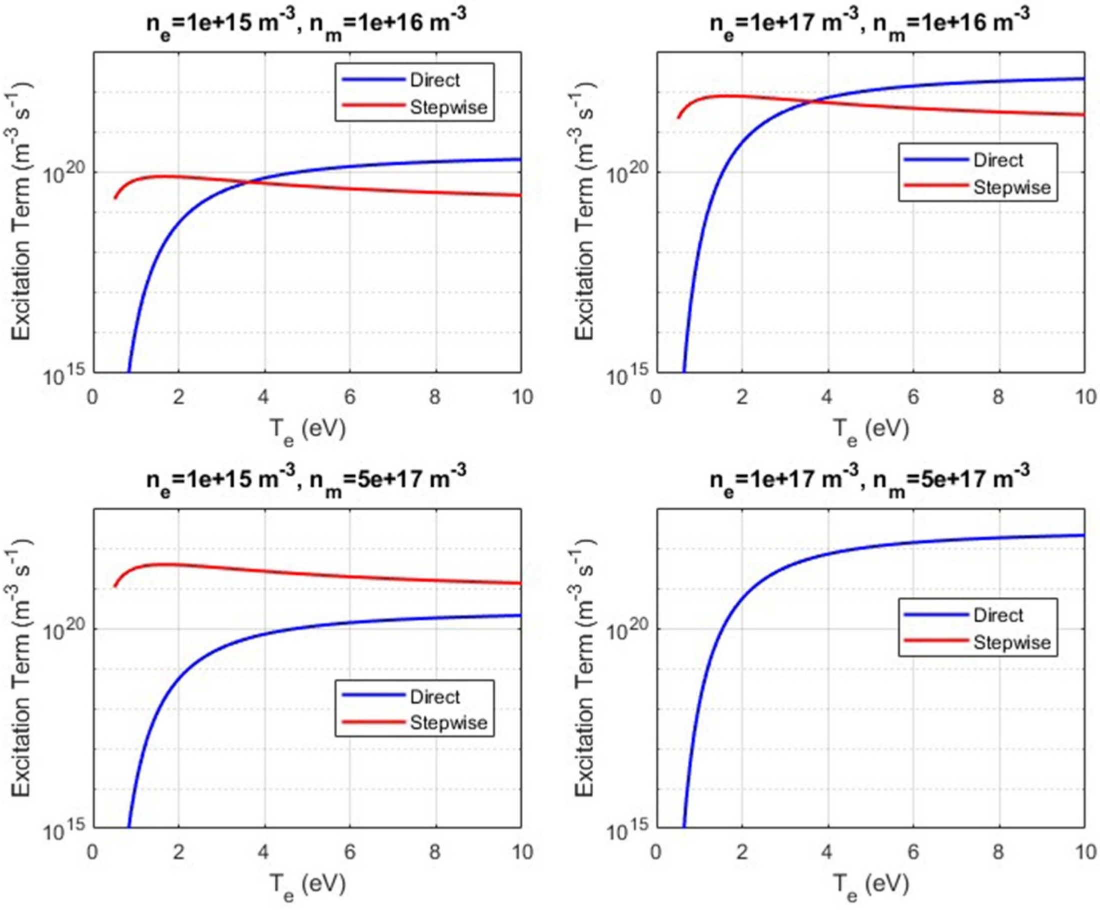

Figure A3. Comparing stepwise excitation from metastable levels versus direct excitation from the ground state.

threshold from the $1s_5$ metastable state. Fractions of electrons within these energy ranges (F_d and F_s, for direct and stepwise, respectively) were computed to assess the EEDF contribution, see figure A2(b), and integrated to the respective rate coefficient $<\sigma\nu>$.

Figure A3 shows the excitation terms on a semi-logarithmic scale versus T_e, with two curves for each n_m and n_e case, each showing direct (solid) and stepwise (dashed) contributions. At low T_e (0.5–3 eV), the stepwise term dominates, particularly for $n_m = 10^{17}$ m^{-3}. For the $n_m = 10^{16}$ m^{-3} case, the direct term overtakes at $T_e > 3.5$ eV, but with $n_m > 10^{17}$ m^{-3} stepwise term stays dominant.

The dominance of stepwise excitation from Ar $1s_5$ metastables challenges the foundational assumption of the corona model, which relies on direct ground-state excitation and neglects other population mechanisms. Literature suggests that ignoring this pathway in the 1–3 Torr regime can lead to T_e underestimations of 20%–50% [72–74].

Although the corona model assumptions do not hold, the 763.51 nm (from the $2p_6$) and the 811.53 nm (from the $2p_9$) line ratio can still serve as a useful qualitative proxy for T_e trends. Both lines are populated from the same Ar $1s_5$ metastable pool, decay to the same 1s manifold, and have closely spaced upper levels with similar excitation cross sections. As a result, stepwise contributions scale comparably and partially cancel in the ratio, preserving the sensitivity to changes in the T_e, see equation (2) in the main text. At 2.6 Torr, other complicating effects such as radiation trapping and collisional quenching are relatively minor for these transitions [60], so the assumptions of this method hold approximately. The observed T_e trends are also consistent with expected behavior, such as the electron cooling seen when CH_4 is added. Taken together, these factors suggest that the chosen line ratio provides a reasonable qualitative indicator of T_e, even though quantitative accuracy would require a full CRM.

For $T_e < 3.5$ eV, the energy distribution predominantly supports stepwise excitation over direct excitation, with a higher electron fraction in the 1.5–1.6 eV range compared to energies above 11.55 eV.

Appendix C

Table A1 summarizes the examination of various NN architectures, and the results reveal a clear trend toward improved performance with increasing model complexity, up to an optimal point beyond which overfitting occurs. Single-layer networks with 10–80 nodes yield high R^2 values (0.996–0.997) but moderate errors (MAPE 3.6–5.0%, MSE ∼0.001), with validation performance ranging from 0.000 87 to 0.0028, peaking at the 40-node architecture. Two-layer models significantly enhance accuracy ($R^2 \geqslant 0.999$, MAPE $< 2.1\%$, MSE < 0.0004), achieving a ValPerf as low as 0.000 44 for [40 20] and [80 40]. Three-layer configurations further refine results, with [50 30 15] delivering the lowest ValPerf among them at 0.00034. Four-layer architectures culminate in the overall best performer, [80 40 20 10] (R^2 0.9998, MAPE 0.74%, MSE 0.000 14, ValPerf 0.000 26), but larger variants like [200 100 50 25] show degraded ValPerf (0.0017), indicating overfitting. The [80 40 20 10] architecture was chosen as optimal, balancing superior fit and generalization without excessive complexity.

Table A1. Varying NN architecture.

Architecture	R^2	MAPE	MSE	ValPerf
10	0.9959	4.6627	0.001 3096	0.001 9221
20	0.995 58	4.8367	0.001 4057	0.001 653
30	0.996 08	5.0318	0.001 0425	0.001 0754
40	0.997 22	3.5607	0.000 81435	0.000 87213
60	0.996 04	3.6127	0.001 2716	0.002 8305
80	0.996 51	4.7674	0.001 2034	0.001 8502
[20 10]	0.995 15	5.4481	0.001 5175	0.001 1854
[30 15]	0.999 15	1.7019	0.000 283 41	0.000 521 75
[40 20]	0.999 24	1.532	0.000 272 29	0.000 435 12
[60 30]	0.999 01	2.1073	0.000 401 42	0.000 453 07
[80 40]	0.999 34	1.3843	0.000 231 03	0.000 446 81
[50 30 15]	**0.999 52**	**1.0287**	**0.000 196 17**	**0.000 338 82**
[80 40 20]	0.999 34	1.4408	0.000 317 55	0.00052822
[100 50 25]	0.999 26	1.1388	0.000 314 55	0.000 740 79
[200 100 50]	0.998 05	1.5009	0.000 754 23	0.001 8307
[80 40 20 10]	**0.999 76**	**0.739 08**	**0.000 141 94**	**0.000 264 06**
[200 100 50 25]	0.998 78	1.1975	0.000 414 78	0.001 6912

References

[1] Askari S, Macias-Montero M, Velusamy T, Maguire P, Svrcek V and Mariotti D 2015 Silicon-based quantum dots: synthesis, surface and composition tuning with atmospheric pressure plasmas *J. Phys. Appl. Phys.* **48** 314002

[2] Nozaki T, Sasaki K, Ogino T, Asahi D and Okazaki K 2007 Silicon nanocrystal synthesis in microplasma reactor *J. Therm. Sci. Technol.* **2** 192–9

[3] Mangolini L, Thimsen E and Kortshagen U 2005 High-yield plasma synthesis of luminescent silicon nanocrystals *Nano Lett.* **5** 655–9

[4] Pi X D and Kortshagen U 2009 Nonthermal plasma synthesized freestanding silicon–germanium alloy nanocrystals *Nanotechnology* **20** 295602

[5] Gresback R, Holman Z and Kortshagen U 2007 Nonthermal plasma synthesis of size-controlled, monodisperse, freestanding germanium nanocrystals *Appl. Phys. Lett.* **91** 093119

[6] Izadi A and Anthony R J 2019 A plasma-based gas-phase method for synthesis of gold nanoparticles *Plasma Process. Polym.* **16** e1800212

[7] Kortshagen U 2016 Nonthermal plasma synthesis of nanocrystals: fundamentals, applications, and future research needs *Plasma Chem. Plasma Process.* **36** 73–84

[8] Gogoi P, Dixit P and Agarwal P 2007 Amorphous silicon films with high deposition rate prepared using argon and hydrogen diluted silane for stable solar cells *Sol. Energy Mater. Sol. Cells* **91** 1253–7

[9] Uner N B, Niedzwiedzki D M and Thimsen E 2019 Nonequilibrium plasma aerotaxy of InN nanocrystals and their photonic properties *J. Phys. Chem. C* **123** 30613–22

[10] Ho A, Mandal R, Lunt R R and Anthony R J 2021 Nonthermal plasma synthesis of gallium nitride nanoparticles: implications for optical and electronic applications *ACS Appl. Nano Mater.* **4** 5624–9

[11] Thimsen E, Kortshagen U R and Aydil E S 2015 Nonthermal plasma synthesis of metal sulfide nanocrystals from metalorganic vapor and elemental sulfur *J. Phys. Appl. Phys.* **48** 314004

[12] Woodard A, Xu L, Barragan A A, Nava G, Wong B M and Mangolini L 2018 On the non-thermal plasma synthesis of nickel nanoparticles *Plasma Process. Polym.* **15** 1700104

[13] Anthony R and Kortshagen U 2009 Photoluminescence quantum yields of amorphous and crystalline silicon nanoparticles *Phys. Rev. B* **80** 115407

[14] Mangolini L and Kortshagen U 2007 Plasma-assisted synthesis of silicon nanocrystal inks *Adv. Mater.* **19** 2513–9

[15] Exarhos S, Alvarez-Barragan A, Aytan E, Balandin A A and Mangolini L 2018 Plasmonic core–shell zirconium nitride–silicon oxynitride nanoparticles *ACS Energy Lett.* **3** 2349–56

[16] Mandal R, O'Shea K and Anthony R 2018 Silicon nitride-capped silicon nanocrystals via a nonthermal dual-plasma synthesis approach *J Vac. Sci. Technol. A* **36** 051303

[17] Dsouza S D, Buerkle M, Alessi B, Brunet P, Morelli A, Payam A F, Maguire P, Mariotti D and Svrcek V 2023 Synthesis of water-stable and highly luminescent graphite quantum dots *Nanotechnology* **34** 505601

[18] Djerourou S, Djebli M and Ouchabane M 2019 Plasma parameters of RF capacitively coupled discharge: comparative study between a plane cathode and a large hole dimensions multi-hollow cathode *Eur. Phys. J. Appl. Phys.* **85** 10801

[19] Bogaerts A, Neyts E, Gijbels R and van der Mullen J 2002 Gas discharge plasmas and their applications *Spectrochim. Acta B* **57** 609–58

[20] Perrin J, Bohm C, Etemadi R and Lloret A 1994 Possible routes for cluster growth and particle formation in RF silane discharges *Plasma Sources Sci. Technol.* **3** 252

[21] Sansonnens L, Howling A A, Hollenstein C, Dorier J L and Kroll U 1994 The role of metastable atoms in argon-diluted silane radiofrequency plasmas *J. Phys. Appl. Phys.* **27** 1406–11

[22] Schröter S, Bahre H, Böke M and Winter J 2014 The role of argon metastables in an inductively coupled plasma for treatment of PET *Plasma Process. Polym.* **11** 239–46

[23] Donkó Z, Hartmann P, Korolov I, Schulenberg D, Rohr S, Rauf S and Schulze J 2023 Metastable argon atom kinetics in a low-pressure capacitively coupled radio frequency discharge *Plasma Sources Sci. Technol.* **32** 065002

[24] Gallagher A 1988 Neutral radical deposition from silane discharges *J. Appl. Phys.* **63** 2406–13

[25] Yatom S, Chopra N, Kondeti S, Petrova T B, Raitses Y, Boris D R, Johnson M J and Walton S G 2023 Measurement and reduction of Ar metastable densities by nitrogen admixing in electron beam-generated plasmas *Plasma Sources Sci. Technol.* **32** 115005

[26] Hebner G A 1996 Spatially resolved, excited state densities and neutral and ion temperatures in inductively coupled argon plasmas *J. Appl. Phys.* **80** 2624–36

[27] Amorim J, Baravian G and Jolly J 2000 Laser-induced resonance fluorescence as a diagnostic technique in non-thermal equilibrium plasmas *J. Phys. Appl. Phys.* **33** R51–R65

[28] Freegarde T G M and Hancock G 1997 A guide to laser-induced fluorescence diagnostics in plasmas *J. Phys. IV* **07** C4–15–C4–29

[29] Crosley D R 1982 Laser-induced fluorescence in spectroscopy, dynamics, and diagnostics *J. Chem. Educ.* **59** 446

[30] Crosley D R 1986 Laser-induced fluorescence measurement of combustion chemistry intermediates *High Temp. Mater. Process.* **7** 41–54

[31] Yatom S 2023 Diagnostics of plasma–liquids systems: challenges and their mitigation *Phys. Plasmas* **30** 033507

[32] Yatom S, Luo Y, Xiong Q and Bruggeman P J 2017 Nanosecond pulsed humid Ar plasma jet in air: shielding, discharge characteristics and atomic hydrogen production *J. Phys. Appl. Phys.* **50** 415204

[33] Yatom S and Dobrynin D 2022 Examination of OH and H_2O_2 production by uniform and non-uniform modes of dielectric barrier discharge in He/air mixture *J. Phys. Appl. Phys.* **55** 485203

[34] Takizawa K, Sasaki K and Kadota K 2001 Correlation between metastable and ground-state fluorine atom densities measured by laser-induced fluorescence and vacuum ultraviolet absorption spectroscopies *Jpn. J. Appl. Phys.* **40** 5130–3

[35] Krychowiak M, Mertens P, König R, Schweer B, Brezinsek S, Schmitz O, Brix M, Samm U and Klinger T 2008 LIF measurements on an atomic helium beam in the edge of a fusion plasma *Plasma Phys. Control. Fusion* **50** 065015

[36] Kondeti V S S K *et al* 2024 Report on laser-induced fluorescence transitions relevant for the microelectronics industry and sustainability applications *J Vac. Sci. Technol. A* **42** 063005

[37] Vekselman V, Gleizer J, Yatom S, Yarmolich D, Gurovich V T, Bazalitski G, Krasik Y E and Bernshtam V 2009 Laser induced fluorescence of the ferroelectric plasma source assisted hollow anode discharge *Phys. Plasmas* **16** 113504

[38] Romadanov I, Raitses Y, Diallo A, Hara K, Kaganovich I D and Smolyakov A 2018 On limitations of laser-induced fluorescence diagnostics for xenon ion velocity distribution function measurements in Hall thrusters *Phys. Plasmas* **25** 033501

[39] Lucca Fabris A, Young C V and Cappelli M A 2015 Time-resolved laser-induced fluorescence measurement of ion and neutral dynamics in a Hall thruster during ionization oscillations *J. Appl. Phys.* **118** 233301

[40] Diallo A, Keller S, Shi Y, Raitses Y and Mazouffre S 2015 Time-resolved ion velocity distribution in a cylindrical Hall thruster: heterodyne-based experiment and modeling *Rev. Sci. Instrum.* **86** 033506

[41] Goeckner M J, Goree J and Sheridan T E 1992 Measurements of ion velocity and density in the plasma sheath *Phys. Fluids B* **4** 1663–70

[42] Kelly R F, Meaney K D, Gilmore M, Desjardins T R and Zhang Y 2016 ArI/ArII laser induced fluorescence system for measurement of neutral and ion dynamics in a large scale helicon plasma *Rev. Sci. Instrum.* **87** 11E560

[43] Nikolić M, Newton J, Sukenik C I, Vušković L and Popović S 2015 Measurements of population densities of metastable and resonant levels of argon using laser induced fluorescence *J. Appl. Phys.* **117** 023304

[44] Tsuchida K 1984 Density measurement of helium metastable atoms in a plasma by the laser-induced fluorescence method *Jpn. J. Appl. Phys.* **23** 338

[45] Heywood M S, Taylor N and Farnsworth P B 2011 Measurement of helium metastable atom densities in a plasma-based ambient ionization source *Anal. Chem.* **83** 6493–9

[46] Chouteau S, Durocher-Jean A, Granier A, Richard-Plouet M and Stafford L 2024 Time-resolved analysis of Ar metastable and electron populations in low-pressure misty plasma processes using optical emission spectroscopy *Plasma Sources Sci. Technol.* **33** 075016

[47] Lin L, Gershman S, Raitses Y and Keidar M 2023 Data-driven prediction of the output composition of an atmospheric pressure plasma jet *J. Phys. Appl. Phys.* **57** 015203

[48] Van Der Gaag T, Nezu A and Akatsuka H 2023 Partial EEDF analysis and electron diagnostics of atmospheric-pressure argon and argon–helium DBD plasma *J. Phys. Appl. Phys.* **56** 304001

[49] Bonzanini A D, Shao K, Graves D B, Hamaguchi S and Mesbah A 2023 Foundations of machine learning for low-temperature plasmas: methods and case studies *Plasma Sources Sci. Technol.* **32** 024003

[50] Laux C O, Spence T G, Kruger C H and Zare R N 2003 Optical diagnostics of atmospheric pressure air plasmas *Plasma Sources Sci. Technol.* **12** 125

[51] Gershman S, Shneider M and Raitses Y 2025 Decomposition of methane diluted with inert gas in an RF discharge cell *J. Phys. D: Appl. Phys.* accepted (https://doi.org/10.1088/1361-6463/ae2927)

[52] Nikhar T, Basu S, Abe S, Yatom S, Raitses Y, Anthony R and Baryshev S V 2024 Importance of gas heating in capacitively coupled radiofrequency plasma-assisted synthesis of carbon nanomaterials *J. Phys. Appl. Phys.* **57** 475205

[53] Godyak V 2021 RF discharge diagnostics: some problems and their resolution *J. Appl. Phys.* **129** 041101

[54] Dosbolayev M K, Orazbayev S A, Boufendi L, Ramazanov T S and Boeuf J P 2024 New insights in the stratification of an argon positive column plasma. II. Experiments and particle simulations *Phys. Plasmas* **31** 073509

[55] Wiechula J, Schönlein A, Iberler M, Hock C, Manegold T, Bohlender B and Jacoby J 2016 Electron density and plasma dynamics of a colliding plasma experiment *AIP Adv.* **6** 075313

[56] Snyder S C, Reynolds L D, Fincke J R, Lassahn G D, Grandy J D and Repetti T E 1994 Electron-temperature and electron-density profiles in an atmospheric-pressure argon plasma jet *Phys. Rev. E* **50** 519–25

[57] Melnikov A D, Usmanov R A, Gavrikov A V, Liziakin G D, Smirnov V P, Timirkhanov R A and Vorona N A 2019 Application of line-intensity-ratio method for measurement of electron temperature of radio-frequency plasma of argon in magnetic field inside the plasma separator *J. Phys.: Conf. Ser.* **1147** 012131

[58] Mitic S, Klumov B A, Pustylnik M Y and Morfill G E 2010 Determination of electron temperature in low-pressure plasmas by means of optical emission spectroscopy *JETP Lett.* **91** 231–5

[59] Hutchinson I H 2002 *Principles of Plasma Diagnostics* (Cambridge University Press) (https://doi.org/10.1017/CBO9780511613630)

[60] Jenina Arellano F, Gyulai M, Donkó Z, Hartmann P, Tsankov T V, Czarnetzki U and Hamaguchi S 2023 First-principles simulation of optical emission spectra for low-pressure argon plasmas and its experimental validation *Plasma Sources Sci. Technol.* **32** 125007

[61] Kramida A and Ralchenko Y 1999 *NIST Atomic Spectra Database, NIST Standard Reference Database 78* (National Institute of Standards and Technology) (https://doi.org/10.18434/T4W30F)

[62] Boffard J B, Chiaro B, Weber T and Lin C C 2007 Electron-impact excitation of argon: optical emission cross sections in the range of 300–2500nm *At. Data Nucl. Data Tables* **93** 831–63

[63] Velazco J E, Kolts J H and Setser D W 1978 Rate constants and quenching mechanisms for the metastable states of argon, krypton, and xenon *J. Chem. Phys.* **69** 4357–73

[64] Wilczek S, Schulze J, Brinkmann R P, Donkó Z, Trieschmann J and Mussenbrock T 2020 Electron dynamics in low pressure capacitively coupled radio frequency discharges *J. Appl. Phys.* **127** 181101

[65] Schulze J, Donkó Z, Lafleur T, Wilczek S and Brinkmann R P 2018 Spatio-temporal analysis of the electron power absorption in electropositive capacitive RF plasmas based on moments of the Boltzmann equation *Plasma Sources Sci. Technol.* **27** 055010

[66] Katori H and Shimizu F 1993 Lifetime measurement of the 1_{s5} metastable state of argon and krypton with a magneto-optical trap *Phys. Rev. Lett.* **70** 3545–8

[67] Boffard J B, Piech G A, Gehrke M F, Anderson L W and Lin C C 1999 Measurement of electron-impact excitation cross sections out of metastable levels of argon and comparison with ground-state excitation *Phys. Rev. A* **59** 2749–63

[68] Maloney C M, Peacher J L, Bartschat K and Madison D H 2000 Excitation of Ar 3 p 5 4 s — 3 p 5 4 p transitions by electron impact *Phys. Rev. A* **61** 022701

[69] Bell K L, Scott N S and Lennon M A 1984 The scattering of low-energy electrons by argon atoms *J. Phys. B: At. Mol. Opt. Phys.* **17** 4757

[70] Ferch J, Granitza B, Masche C and Raith W 1985 Electron-argon total cross section measurements at low energies by time-of-flight spectroscopy *J. Phys. B: At. Mol. Opt. Phys.* **18** 967

[71] Song M-Y, Yoon J-S, Cho H, Itikawa Y, Karwasz G P, Kokoouline V, Nakamura Y and Tennyson J 2015 Cross sections for electron collisions with methane *J. Phys. Chem. Ref. Data* **44** 023101

[72] Lee Y-K and Chung C-W 2011 Ionization in inductively coupled argon plasmas studied by optical emission spectroscopy *J. Appl. Phys.* **109** 013306

[73] Rachdi L, Sushkov V and Hofmann M 2022 Optical emission spectroscopy diagnostics for plasma parameters investigation in a Duo-Plasmaline surface-wave sustained discharge *Spectrochim. Acta B* **194** 106432

[74] Horita H, Kuwahara D, Akatsuka H and Shinohara S 2021 Estimating electron temperature and density using improved collisional-radiative model in high-density RF argon plasma *AIP Adv.* **11** 075226

[75] Yatom S *et al* 2025 Data for “Dynamics of Argon Metastables in Ar-CH4 Radio Frequency Capacitively-Coupled Plasma: Real-Time Monitoring with Neural Network-Augmented Broadband Optical Emission Spectroscopy” *Princeton Data Commons: Describe* (https://doi.org/10.34770/3tw2-2k05)